Resolving Ultrasound Contrast Microbubbles using Minimum Variance Beamforming

Diamantis, Konstantinos; Anderson, Tom; Butler, Mairead B. ; Villagómez Hoyos, Carlos Armando; Jensen, Jørgen Arendt; Sboros, Vassilis

Published in:
I E E E Transactions on Medical Imaging

Link to article, DOI:
10.1109/TMI.2018.2859262

Publication date:
2019

Document Version
Peer reviewed version

This article has been accepted for publication in a future issue of this journal, but has not been fully edited. Content may change prior to final publication. Citation information: DOI 10.1109/TMI.2018.2859262, IEEE Transactions on Medical Imaging

Resolving Ultrasound Contrast Microbubbles using Minimum Variance Beamforming

Konstantinos Diamantis, Tom Anderson, Mairead B. Butler, Carlos A. Villagómez-Hoyos, Jørgen Arendt Jensen, *Fellow, IEEE,* and Vassilis Sboros

***Abstract*— Minimum Variance (MV) beamforming is known to improve the lateral resolution of ultrasound images and enhance the separation of isolated point scatterers. This paper aims to evaluate the adaptive beamformer's performance with flowing microbubbles (MBs), which are relevant to super-resolution ultrasound imaging. Simulations using point scatterer data from single emissions were complemented by an experimental investigation performed using a capillary tube phantom and the Synthetic Aperture Real-time Ultrasound System (SARUS). The MV performance was assessed by the minimum distance that allows the display of two scatterers positioned side-by-side, the lateral Full-Width-Half-Maximum (FWHM), and the Peak-Side-lobe-Level (PSL). In the tube, scatterer responses separated by down to 196 μm (or 1.05λ) were distinguished by the MV method, while the standard Delay-and-Sum (DAS) beamformers were unable to achieve such separation. Up to 9-fold FWHM decrease was also measured in favour of the MV beamformer, for individual echoes from MBs. The lateral distance between two scatterers impacted on their FWHM value, and additional differences in the scatterers' axial or out-of-plane position also impacted on their size and appearance. The simulation and experimental results were in agreement in terms of lateral resolution. The point scatterer study showed that the proposed MV imaging scheme provided clear resolution benefits compared to DAS. Current super-resolution methods mainly depend on DAS beamformers. Instead, the use of the MV method may provide a larger number of detected, and potentially better localized, MB scatterers.**

***Index Terms*—Closely-spaced scatterers, microbubbles, Minimum Variance beamforming, lateral resolution, super-resolution ultrasound.**

I. Introduction

In ultrasound imaging, the standard method to process received signals by a transducer array is the Delay-And-Sum (DAS) beamformer [1]. The transducer element signals are time-delayed, weighted, and finally summed to form a maximized output. The weights are usually fixed modified cosine functions that do not depend on the data. The process favours structural/anatomical imaging and not the detection and localization of point scatterers such as contrast microbubbles (MBs) [2]. Adaptive beamforming appears in various applications of array signal processing and is shown to significantly increase directional sensitivity without the requirement to physically move the sensor array [3]. In medical ultrasound, most of the adaptive beamforming research is focused on the Minimum Variance (MV) beamformer [4]. The MV beamformer calculates data-dependent apodization weights aiming to preserve the signal from a desired direction while minimizing all other signal contributions from other directions. A number of studies have shown that the MV method is capable of providing sub-wavelength lateral localization of ultrasound point scatterers [5]–[12], and higher point resolvability compared to the conventional beamformers [6], [13]. Modified MV implementations have been proposed [14]–[16] for real-time applications in vascular imaging [17], corneal wound detection [18], and cardiac imaging [19], [20].

In general, the MV method becomes most effective when the target is a small collection of scatterers, which corresponds to a small number of unknowns. The theoretical basis of this is that there are sufficient degrees of freedom to identify all scatterer locations, in relation to the number of available transducer element signals [6]. On the other hand in the case of an anatomical structure the image is flooded by scatterers, and there are insufficient parameters to resolve all of them [16]. Thus, the literature indicates that MV methods are better suited for imaging point targets as there is consensus that significant lateral resolution gains can be achieved [9]–[12]. This may be beneficial to the recent development in Super-Resolution Imaging (SRI) [21]–[25], which deploys MB localization methods to increase resolution. Techniques have focused on the resolution improvement achievable by imaging single MBs, resulting in images of blood flow dynamics with significantly increased detail.

SRI is largely image-based and it mostly depends on DAS beamformed images. The lateral Full-Width-at-Half-Maximum (FWHM) measured from the Point-Spread-Function (PSF) of a single scatterer is often used as an indicator of the lateral resolution achieved by a beamformer. Given that the MV beamformer may provide FWHM values more than 20-times lower compared to the DAS beamformer [11], [12], it is hypothesized that MV beamforming can resolve more closely spaced MBs compared to the DAS. However, the use of the FWHM is not a direct measurement of lateral resolution as

This work was supported by the Science and Technology Facilities Council (STFC-ST/M007804/1), by grant 82-2012-4 from the Danish Advanced Technology Foundation, and by B-K Ultrasound ApS. *Asterisk indicates corresponding author.*

K. Diamantis, M. B. Butler, and *V. Sboros are with the Institute of Biological Chemistry, Biophysics and Bioengineering (IB3), Heriot-Watt University (HWU), Edinburgh, UK, (e-mail: V.Sboros@hw.ac.uk).

T. Anderson is with the School of Clinical Sciences, Centre of Cardiovascular Science, University of Edinburgh, UK.

C. A. Villagómez-Hoyos and J. A. Jensen are with the Department of Electrical Engineering, Center for Fast Ultrasound Imaging, Technical University of Denmark, Kgs. Lyngby, Denmark.

This article has been accepted for publication in a future issue of this journal, but has not been fully edited. Content may change prior to final publication. Citation information: DOI 10.1109/TMI.2018.2859262, IEEE Transactions on Medical Imaging

the interactions between scatterers may alter its value. Key to this hypothesis testing is a quantitative assessment of the lateral resolution based on the classical definition; that is the smallest possible distance between two point sources, located side-by-side that enables the display of two points as separate targets [26]. Single emission beamformed responses are used as they can significantly increase the acquisition rate without sacrificing resolution [9], [10], and are relevant to imaging fast-moving targets like MBs that are used in SRI [22]–[24].

II. Methods

A. Minimum Variance Beamforming

1) MV Beamformer Output: The MV beamformer has been described previously in [6]–[8]. Briefly, the processing involves the estimation of the sample covariance matrix $\hat{\boldsymbol{R}}(t)$, and the transducer array division into overlapping sub-arrays of length, L. The output $B(t,\vec{p})$ of the MV beamformer for a probe with M transducer elements, which are all used in receive, for a point located at the position $\vec{p}$, and for a single emission, is given by:

$$B(t,\vec{p}) = \frac{1}{M-L+1}\sum_{l=0}^{M-L} \boldsymbol{w}(t)^H \boldsymbol{X}_l(t)\,, \tag{1}$$

where t is the time vector, $\boldsymbol{w}(t)$ is the vector of the adaptive weights, $\boldsymbol{X}_l(t)$ is the set of the transducer element signals from the lth sub-array $[x_l(t), x_{l+1}(t), ..., x_{l+L-1}(t)]^H$, and $\{.\}^H$ denotes the conjugate transpose. The MV apodization weights are calculated by:

$$\boldsymbol{w}(t) = \frac{\hat{\boldsymbol{R}}(t)^{-1}\boldsymbol{e}}{\boldsymbol{e}^H\hat{\boldsymbol{R}}(t)^{-1}\boldsymbol{e}}\,, \tag{2}$$

where $\boldsymbol{e}$ is the time-delay vector, and $\hat{\boldsymbol{R}}(t)$ is given by:

$$\hat{\boldsymbol{R}}(t) = \frac{1}{M-L+1}\sum_{l=0}^{M-L} \boldsymbol{X}_l(t)\boldsymbol{X}_l(t)^H\,. \tag{3}$$

2) MV Beamforming for Point Scatterer Imaging: Substantial previous work has established an optimization methodology for use of the MV beamformer in the imaging of point scatterers [9], [10], [12]. This work alongside with other MV studies [6]–[8], [16], [27] has helped develop the MV beamformer, by investigating the impact of all MV-related parameters in the imaging of point scatterers. This knowledge was implemented here to maximize MV performance in the present ultrasound datasets. Specifically to obtain a more robust covariance matrix estimate, a diagonal loading technique as in [6] was employed. Further, a Forward-Backward (FB) averaging technique as in [27] was also used to allow the inversion of the sample covariance matrix for a larger sub-array length value, $L \approx 2M/3 = 80$ as in [12]. The latter inherently increases the maximum achievable resolution. Hence, $\hat{\boldsymbol{R}}'(t)$ was used in (2) instead of $\hat{\boldsymbol{R}}(t)$ that is given by:

$$\hat{\boldsymbol{R}}'(t) = \frac{1}{2}\left(\hat{\boldsymbol{R}}(t) + J\hat{\boldsymbol{R}}(t)^H J + \frac{1}{L}\mathrm{Tr}\{\hat{\boldsymbol{R}}(t)\}\right), \tag{4}$$

where J is the exchange matrix and Tr is the matrix trace. The MV method was then used to beamform a single emission image [9], [10], by calculating an apodization weight for each pixel [16]. The pixel dimensions were 12.5 μm by 25 μm, with smaller lateral size that improves MV resolution [12]. In addition, Boxcar and Hanning [28] apodization weights were also applied to form DAS beamformed images for comparison. For these, a fixed receive aperture was employed.

B. Ultrasound Data Acquisition

1) Imaging Setup: A 128-element linear array transducer with a 8 MHz centre frequency (f_0) and 1.5λ pitch was used to scan a number of simulated point scatterer phantoms and a custom phantom with MBs flowing inside a tube. In transmission, transducer elements #33 to #96 were employed to emit a spherical wave. The F-number was -3.5 and Hanning apodization was also used to reduce edge waves [29]. The negative F-number refers to a virtual source positioned behind the transducer central element (#64) [30], [31]. The excitation function was a sinusoid at f_0, also weighted by a 50% Tukey window. The RF data from each emission were acquired from all transducer elements individually in receive. The scanning parameters were similar for simulations and measurements, and 10 individual tube phantom frames have been produced in this way.

2) Simulations: The ultrasound field simulation package Field II [32], [33] was used to initially evaluate the lateral resolution limit of the MV beamformer. First a single scatterer was positioned at $(x,y,z) = (0,\ 0,\ 70)$ mm, where x, y, z correspond to the lateral, out-of-plane, and axial direction respectively. Next, a number of phantoms were created, consisting of 2 point scatterers at the same depth (z) and positioned side-by-side in the lateral direction. The smallest lateral distance separating the two scatterers was 100 μm and their positions were ($\pm$0.05,0,70) mm. The distance was increased with a step of 25 μm between successive simulations, until clear scatterer separation was achieved. The speed of sound, c was set to 1540 m/s, resulting in a wavelength $\lambda = 192.5$ μm, and the sampling frequency, f_s was 100 MHz. The simulations were repeated for depths between 40 mm and 100 mm with a 10 mm step to match the depth range of the experiment. The behaviour of the MB scatterers was not simulated but their brightness and Signal-to-Noise-Ratio (SNR) were made similar to that of the experiment. In Field II this was achieved by introducing a strong reflector elsewhere in the image. Finally, additional simulations involving scatterer separation in the z-range (0.1 mm) and y-range (1 mm), on top of the x-range, were also performed in an attempt to investigate possible causes of PSF distortion observed in the experimental data.

3) Experimental Setup: A setup was used to allow individual MBs to be distinguished in the image as described in earlier work [34]. The schematic representation of the experimental setup is shown in Fig. 1. The measurements were performed by the 1024 channel experimental ultrasound scanner SARUS [35]. The speed of sound, c was measured based on the water temperature [36], resulting in a wavelength $\lambda = 186$ μm. The data were sampled at 35 MHz. The phantom consisted of a water tank in which a cellulose capillary tube with 200 μm nominal internal diameter was mounted. The capillary tube was taken from a single dialysis cartridge (Fiber Dialyzer GFE-09, Gambro, Germany). The tube diameter was inspected prior to the experiment under a microscope and it

This article has been accepted for publication in a future issue of this journal, but has not been fully edited. Content may change prior to final publication. Citation information: DOI 10.1109/TMI.2018.2859262, IEEE Transactions on Medical Imaging

was found to be 400 μm at maximum. The tube was chosen after the simulation had shown that the resolution of the MV is below its diameter, while the DAS beamformer could not resolve MBs within this range. Possible tube bending during the mounting procedure may have allowed for higher distances between scatterers. The tube was connected through additional tubing to an infusion pump containing the MB suspension. The MBs used for this experiment were custom made lipid-shelled that contain per-fluorocarbon gas and their diameter varied between $1-10$ μm [37]. Such MBs have been previously shown to provide reproducibly strong scattering events for minutes to hours in suspension [38]. The infusion pump contained 0.1 mL of MB solution mixed with 150 mL of water, and the rate of infusion was 5.6 mL/hour to provide a sparse MB population in the captured image. Much higher MB concentrations provided strong echoes, and thus a bright image along the tube, which was initially used to align the transducer with the tube. The imaging sequence, also described in [39] provided a Mechanical Index (MI) that dropped as depth increased and it was lower than 0.3 for the scanning depths of the present study (between 49 mm and 81 mm), which minimized MB destruction.

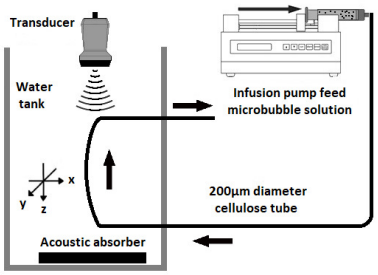

Fig. 1. Illustration of the experimental setup for microbubble localization. The transducer acquired the data from MBs that were located in the parabolic part of the tube in the centre of the tank.

C. Data Analysis

The lateral FWHM and the Peak-Sidelobe-Level (PSL) were measured both from simulated and MB scatterers, for each beamformer. The lateral FWHM is defined as the width (in μm) of the main lobe from the PSF of the single scatterer, and the PSL is the peak value of the first side-lobe (in dB) [12]. The positioning of simulated scatterers side-by-side and the choice of capillary tube width during the MB data acquisition enabled a comparison between beamformers in terms of lateral resolution. The classical lateral resolution definition [26] was deployed in a quantitative manner. For two neighbouring scatterers at a specific depth, the scatterer separation first becomes visible with the appearance of a second peak from the power variation. In this work, the -3 dB power drop between the two peaks, was defined as the critical separation limit (S_{-3dB}). Likewise, the -6 dB power drop between the two peaks was defined as significant separation limit (S_{-6dB}), that enables the FWHM measurement in each of the scatterers (without using lobe extrapolation). Note that it is not possible to make a direct and reliable FWHM measurement for 2 scatterers that are separated by less than -6 dB power drop between them.

III. Results

A. Simulation

Fig. 2 shows the beamformed responses of a simulated pair of scatterers at 70 mm depth, apart from the 1^{st} row where a single scatterer is displayed. Fig. 2(a) and (b) show results for the DAS while the remainder of the figure shows the results for the MV beamformer. In the 2^{nd} row of Fig. 2(a)-(c) the two scatterers were laterally separated by 100 μm (or $\approx \lambda/2$), and in the 3^{rd} row by 275 μm. In both cases all the images shown in Fig. 2(a)-(c) and for all beamformers, appeared to include a single scatterer. The 275 μm distance was the greatest before any scatterer separation (power drop) was visible. The values of the FWHM and the PSL for the scatterers in the first 3 rows of Fig. 2(a)-(c) are displayed in Table I. The lowest FWHM value was achieved in the single scatterer case by the MV beamformer, where the measured 71.9 μm (or 0.37λ) correspond to a 6.3-fold improvement compared to the best DAS beamformer (Boxcar). The lowest PSL was found for the MV beamformer, where the measured -41.7 dB indicate a -7.8 dB contrast improvement compared to the best DAS (Hanning). Table I also shows that there is 5.2-fold FWHM variability in the MV beamformer, between a single scatterer (71.9 μm) and two overlapping ones that appear as single (375.5 μm). Hence, any FWHM value within this range (71.9 μm$-$375.5 μm) can be measured from what may appear as a single scattering event, using the MV beamformer. The DAS Boxcar responses provided FWHM values between 455.8 μm and 523.9 μm. This resulted in varying resolution gains using the MV beamformer compared to the best DAS (Boxcar), between 6.3-fold (single scatterer) and 1.4-fold (merged double scatterers) at 70 mm depth. In the last 3 rows of Fig. 2(a)-(c) the lateral distances between the two scatterers were increased to 350 μm, 400 μm and 575 μm respectively, resulting in scatterer separation using the MV beamformer, at first critical (4^{th} row) and more significant at greater distances (rows $5-6$). The DAS Boxcar beamformer achieved critical separation for the greatest lateral distance displayed in Fig. 2(a)-(c) (6^{th} row), while in all other rows the two scatterers were not separated. Hence, the S_{-3dB} as defined in Subsection II-C, was reduced by 1.17λ (or by 39%) for the MV (350 μm) compared to the best DAS (Boxcar, 575 μm). Similarly, the S_{-6dB} was 400 μm (2.08λ) for the MV beamformer while it was 625 μm (3.25λ) for DAS Boxcar, which was a 1.17λ (or 36%) lateral resolution improvement.

Fig. 2(d) shows the MV beamformed responses with identical lateral distances to those of Fig. 2(c), and in addition the only scatterer (1^{st} row) or the second scatterer on the right (rows $2-6$) was positioned at depth of 70.1 mm instead of 70 mm. There were minor metrics differences ($< 10\%$) between the PSFs displayed in the two columns, in the case of a single scatterer (1^{st} row) and for larger lateral separations (rows $5-6$). In the 2^{nd} row, a merged scatterers' echo was seen both in Fig. 2(c) and (d), and in (d) the echo was slightly tilted, and axially longer by 15%, which represented the 0.1 mm of pulse duration added. In the 3^{rd} row, the tilt remained and there were high side-lobes not allowing to determine the number of scatterers in the image (Fig. 2(d)), while a comparison

This article has been accepted for publication in a future issue of this journal, but has not been fully edited. Content may change prior to final publication. Citation information: DOI 10.1109/TMI.2018.2859262, IEEE Transactions on Medical Imaging

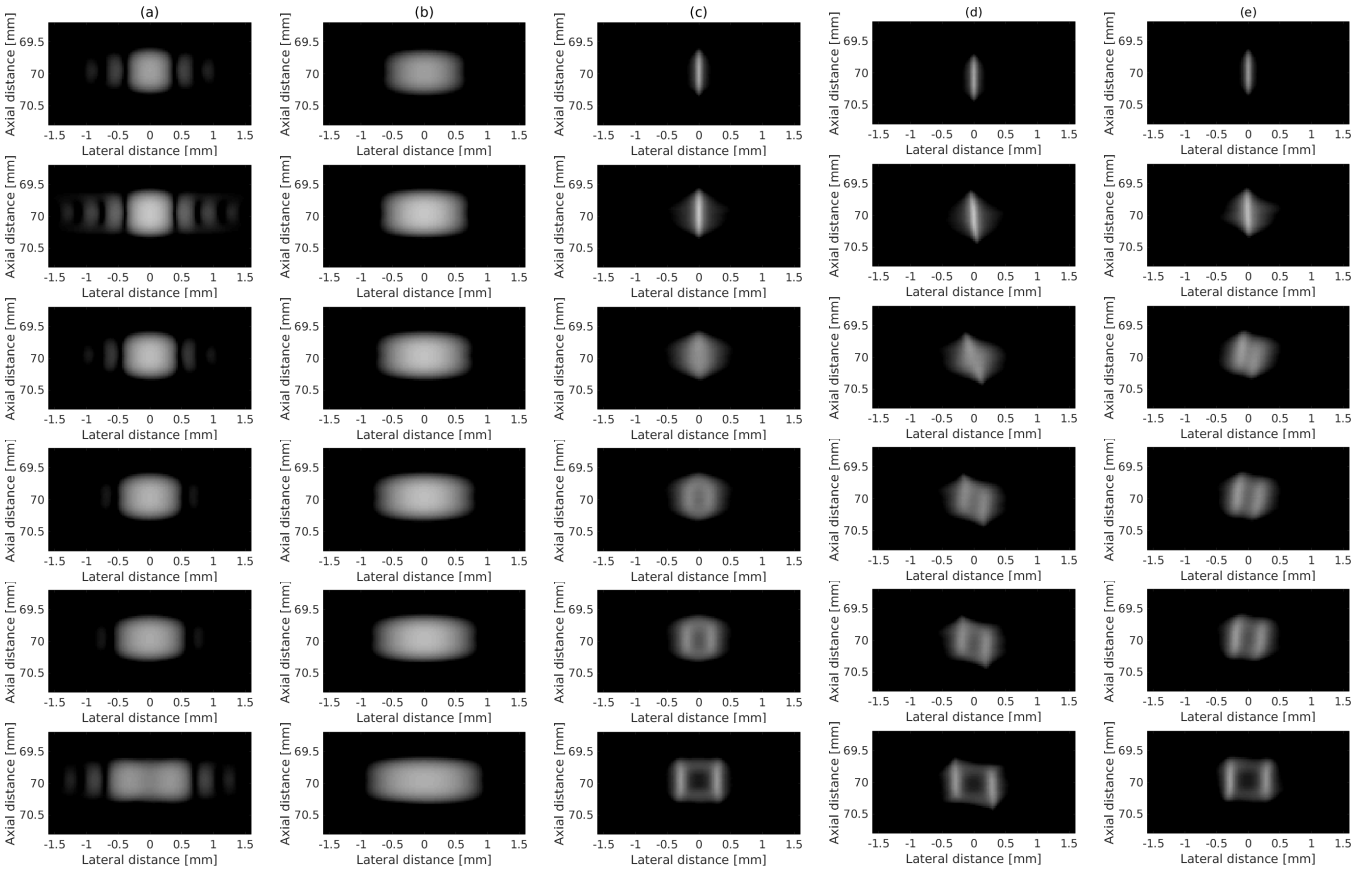

Fig. 2. Beamformed responses of Field II simulated scatterer(s) at 70 mm depth with (a) DAS Boxcar, (b) DAS Hanning, (c) MV apodization, (d) MV apodization including a 0.1 mm z-range scatterer displacement, and (e) MV apodization including a 1 mm y-range scatterer displacement. A single scatterer was simulated in the 1^{st} row. In the following rows two scatterers were separated laterally by 100 μm (2^{nd} row), 275 μm (3^{rd} row), 350 μm (4^{th} row), 400 μm (5^{th} row) and 575 μm (6^{th} row). The dynamic range of the display was 40 dB.

between the 4^{th} row in Fig. 2(c) and (d) showed that the two scatterers due to their overall greater distance can be more easily distinguished in Fig. 2(d).

Fig. 2(e) shows the equivalent to Fig. 2(c) MV beamformed responses, where the only scatterer (1^{st} row) or the scatterer on the right (rows $2-6$) was moved 1 mm in the y-direction compared to the one on the left. A quantitative comparison of the first 2 rows between Fig. 2(c) and (e) showed no significant difference. However, as the Euclidean distance between the two scatterers increased, the scatterers separated and "PSF tilting" was observed for both scatterers (rows $3-5$). In the 3^{rd} row of Fig. 2(e), two point scatterer echoes were visible at 275 μm lateral distance, while this was not possible in Fig. 2(c). In the next two rows of Fig. 2(e) where the lateral separation was larger, the tilt angle reduced with increasing distance, and by the last row the scatterers did not appear different to the last row of Fig. 2(c). Compared to the images shown in Fig. 2(a)-(b), the DAS results were not significantly different for the z- and y-displacements studied here, and thus were not displayed.

The power in dB (y-axis) for the different lateral positions (x-axis) at 70 mm depth is shown in Fig. 3. The number of peaks may provide a criterion for scatterer separation and the power drop where the gap of separation is possible to observe, is an indicator of the separation that each beamforming method can achieve. Fig. 4 shows the maximum power drop between two simulated point scatterers plotted over the lateral distance that separates them. Below a lateral separation distance all methods resulted in a single scatterer image. The lowest separation was achieved by the MV beamformer and was 300 μm (1.56λ). The separation of scatterers became more prominent, i.e. the power drop increased, as their distance increased. The behaviour of the DAS beamformers was similar, but shifted to larger lateral distances. The equivalent limits for DAS Boxcar and Hanning beamformers were 500 μm (2.60λ) and 650 μm (3.38λ) respectively.

Fig. 5 displays the monotonic increase of the FWHM as lateral separations decreased for distances below 1 mm and down to the smallest distance that the FWHM is possible to measure. The FWHM increased from 89.7 μm (1 mm lateral separation) to 227.1 μm (at 400 μm separation or S_{-6dB}), i.e. a 2.5-fold increase. At larger distances it converges to the FWHM value of a single scatterer (71.9 μm). The results were similar when the z- and y-range displacements were also accounted for, with the FWHM values ranging between 84.4 μm (1 mm lateral separation) and 245.3 μm (at 400 μm lateral separation), and between 84.8 μm (1 mm lateral separation) and 206.4 μm (at 350 μm lateral separation) for the left scatterer in Fig. 2(d) and (e) respectively. The FWHM values were similar ($\pm$8%) in the z-displacement case

This article has been accepted for publication in a future issue of this journal, but has not been fully edited. Content may change prior to final publication. Citation information: DOI 10.1109/TMI.2018.2859262, IEEE Transactions on Medical Imaging

TABLE I
PSL AND FWHM, FROM DIFFERENT BEAMFORMED RESPONSES AT 70 mm DEPTH WHERE $\lambda = c/f_0 = 192.5$ μm.

	Single scatterer		Two scatterers separated by 100 μm		Two scatterers separated by 275 μm	
	PSL	FWHM	PSL	FWHM	PSL	FWHM
DAS Boxcar	−14.9 dB	455.8 μm (2.37λ)	−15.5 dB	463.2 μm (2.41λ)	−20.5 dB	523.9 μm (2.72λ)
DAS Hanning	−33.9 dB	730.7 μm (3.80λ)	−34.2 dB	747.6 μm (3.88λ)	−39.3 dB	791.2 μm (4.11λ)
MV	−41.7 dB	71.9 μm (0.37λ)	−43.6 dB	83.6 μm (0.43λ)	−41.1 dB	375.5 μm (1.95λ)

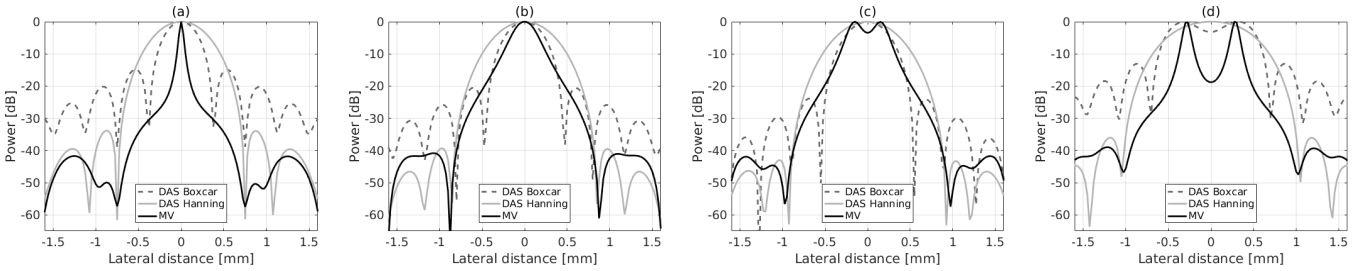

Fig. 3. Lateral variations at 70 mm depth of the beamformed responses of Fig. 2(a)-(c) for (a) a single scatterer, two scatterers separated laterally by (b) 275 μm , (c) 350 μm, and (d) 575 μm.

compared to the standard MV result, while the FWHM was found 5%-30% lower in the y-range case, due to the increased distance separating the two scatterers.

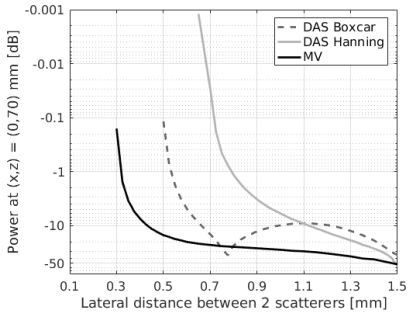

Fig. 4. Variation of maximum power drop between two scatterers at $(x,z) = (0,70)$ mm as a function of their lateral separation distance. The simulated scatterers were positioned symmetrically around $x = 0$.

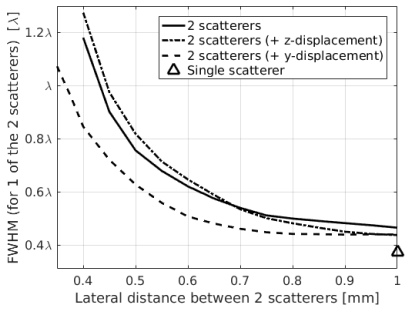

Fig. 5. FWHM measured from one of two closely spaced simulated scatterers as a function of the lateral distance separating them. The MV beamformer was considered and the triangle indicates the FWHM measured from a single scatterer as shown in Fig. 2(c), 1^{st} row.

The above processing was repeated for all depths between 40 mm and 100 mm. In Fig. 6(a) the single scatterer provided a low FWHM variation with depth between 71.9 μm (or 0.37λ) and 99.2 μm (or 0.52λ) for the MV processing. The corresponding values from the best DAS beamformer (Boxcar) were between 310.6 μm (or 1.61λ) and 633 μm (or 3.29λ), increasing monotonically with depth due to the fixed receive aperture used here. These results demonstrate a 3.1- and up to 7.8-fold improvement in favour of the MV method. Fig. 6(b) presents the measured FWHM from two scatterers separated by 100 μm. The FWHM ranged between 81 μm (or 0.42λ) and 131.5 μm (or 0.68λ) for the MV, and between 321.8 μm (or 1.67λ) and 638.1 μm (or 3.31λ) for the DAS Boxcar. The two scatterers were marginally distinguished only at 40 mm depth using the MV beamformer, where a power drop of -0.05 dB was noticed in $(x,z) = (0,40)$ mm. Thus, it was incorrect to measure a single FWHM at this depth, and the lowest measurement depth was at 50 mm where the pair of scatterers appear as single for the MV beamformer. Importantly no power drop was made visible for distances < 100 μm (or $\approx \lambda/2$). In Fig. 6(c), the two scatterers were separated by varying lateral distances equivalent to the S_{-6dB} in each case, and the FWHM was measured in one of the two. In this case, the MV beamformer resulted in FWHM values between 165.9 μm (or 0.86λ) and 310.1 μm (or 1.61λ), while the DAS Boxcar provided FWHM between 350.8 μm (or 1.82λ) and 706.5 μm (or 3.67λ). The FWHM here correlated with depth for all beamformers.

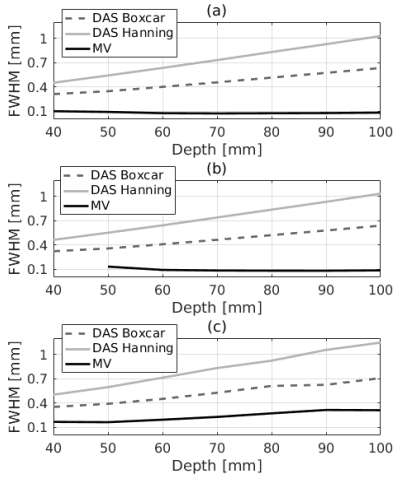

Fig. 6. FWHM variation as a function of depth for DAS and MV responses, in case of (a) a single scatterer, (b) two scatterers separated laterally by 100 μm, and (c) of one of the two scatterers separated by the S_{-6dB}.

In Fig. 7 the PSL variation is shown with respect to depth.

This article has been accepted for publication in a future issue of this journal, but has not been fully edited. Content may change prior to final publication. Citation information: DOI 10.1109/TMI.2018.2859262, IEEE Transactions on Medical Imaging

Fig. 7(a) refers to a single scatterer. The MV responses provided a monotonic PSL decrease with depth between -32 dB and -54 dB, while the best DAS (Hanning) provided a fairly constant PSL at all depths, (-32 dB to -34 dB). Therefore, up to 20 dB contrast improvement was found using the MV beamformer, particularly at greater depths. Fig. 7(b) refers to two scatterers separated by 100 μm. The two scatterers were perceived as one in all but the shortest depth (40 mm) using the MV beamformer, and PSL values between -39 dB and -55 dB were measured for the MV beamformer, while values around -34 dB were measured for DAS Hanning. This result is very close to the single scatterer case in Fig. 7(a). In Fig. 7(c), the two scatterers were further separated to achieve the -6 dB power drop between them. The MV beamformer resulted in PSL values between -31 dB and -42 dB, without a specific trend, while the DAS Hanning provided PSL between -30 dB and -34 dB.

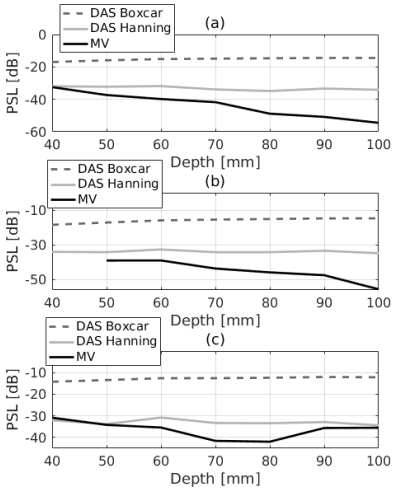

Fig. 7. PSL variation as a function of depth for DAS and MV responses, in case of (a) a single scatterer, (b) two scatterers separated laterally by 100 μm, and (c) of one of the two scatterers separated by the S_{-6dB}.

In Fig. 8 the resolving capability of each beamformer is shown with respect to depth. Fig. 8(a) shows that the S_{-3dB} increased monotonically with depth for all beamformers. Lower values, thus highest resolving capability, were reported closer to the transducer's surface (40 mm depth). Using the MV beamformer, the S_{-3dB} ranged between 175 μm (or 0.91λ) and 525 μm (or 2.73λ). The corresponding values for the best DAS beamformer (Boxcar) were between 400 μm (or 2.08λ) and 800 μm (or 4.16λ), which is an up to $\approx 1.5\lambda$ improvement for the MV beamformer. Similarly, in Fig. 8(b), the S_{-6dB} increased monotonically with depth for all beamformers. For the MV beamformer, the separation limit was between 250 μm (or 1.3λ) and 575 μm (or 2.99λ), and for the DAS Boxcar were between 425 μm (or 2.21λ) and 875 μm (or 4.54λ). Overall, the S_{-6dB} was also reduced by up to 1.5λ, when using the MV beamformer.

B. Tube Phantom Experiment with Microbubbles Flow

The beamformed responses of a single MB phantom frame are shown in Fig. 9 using a 40 dB dynamic range. The

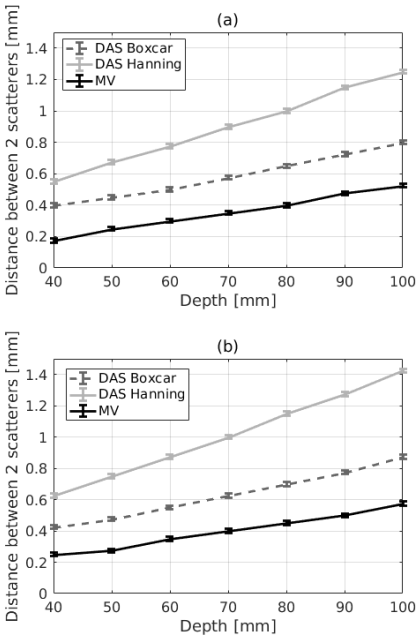

Fig. 8. (a) Critical (S_{-3dB}) and (b) significant (S_{-6dB}) separation limits as a function of depth for 2 simulated scatterers positioned side-by-side. All values are subject to a 25 μm error, which is the step between successive simulations as described in subsection II-B2.

MB stream confined within the tube appeared thinner in the MV case (Fig. 9(c) compared to DAS Boxcar or Hanning (Figs. 9(a) and 9(b)). This implies an improvement of lateral resolution as expected. Further, additional unwanted reflections appearing in the first two subfigures of Fig. 9 (at depth of 70 mm and for a lateral distance between 0 mm and 5 mm) were minimized in the MV image. At the top of the images (between 49 mm and 60 mm depths) the concentration of the contrast agents was higher. This is due to the higher acoustic pressure, which results in a larger number of MBs that provide a scattered signal above the noise level [2].

Thus, as the acoustic pressure drops with depth, it became easier to visualize individual echoes from MBs below 67 mm. In Fig. 10 (rows $1-2$), two examples of possible single MB events are displayed separately for more detail. The values of the FWHM and the PSL for these isolated echoes and for both conventional and adaptive apodization weights are shown in Table II. The echoes were not as symmetric as in Fig. 2 and the FWHM and PSL were averaged over a 0.2 mm depth range around their centre. The lowest FWHM value was 82.7 μm (or 0.44λ) and was achieved by the MV beamformer at 79.4 mm depth, which is a ≈ 9-fold improvement compared to the DAS Boxcar beamformer (743.1 μm or 4λ). For the same MB echo, the PSL was -18.9 dB for the best DAS beamformer (Hanning) while the MV beamformer provided PSL improvement by -3.6 dB (-22.5 dB). Note that although the two scatterers displayed in rows $1-2$ of Fig. 10 are positioned at similar depth (79.2 mm and 79.4 mm), the metrics shown in Table II vary significantly from each other, for all beamformers. The simulation study above has shown that this may be due to a double (or multiple) scattering event that appears as one.

This article has been accepted for publication in a future issue of this journal, but has not been fully edited. Content may change prior to final publication. Citation information: DOI 10.1109/TMI.2018.2859262, IEEE Transactions on Medical Imaging

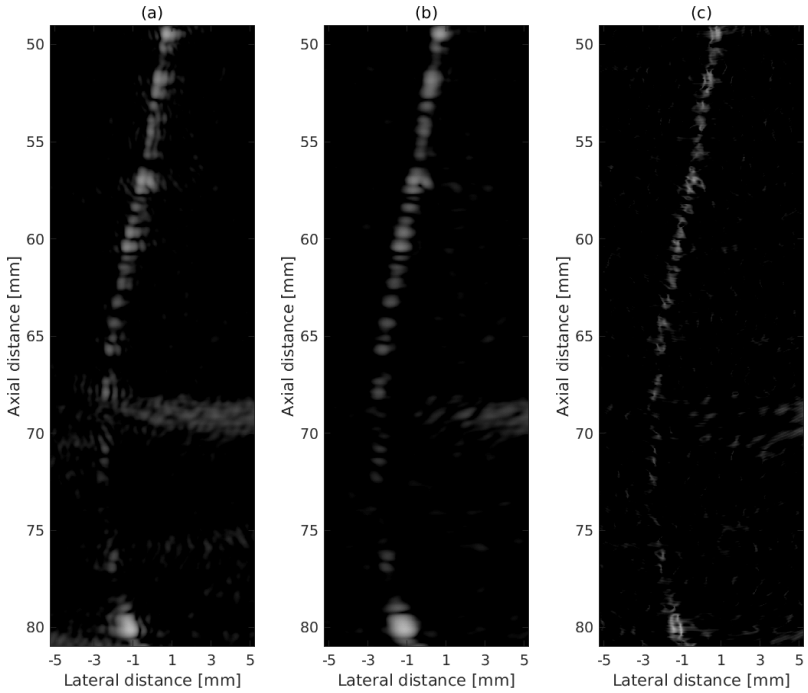

Fig. 9. Beamformed responses of microbubbles inside a cellulose capillary tube with (a) DAS Boxcar, (b) DAS Hanning, and (c) MV apodization. The dynamic range of the display was 40 dB.

TABLE II
PSL AND FWHM, FROM THE BEAMFORMED RESPONSES DISPLAYED IN FIG. 10, WHERE $\lambda = c/f_0 = 186$ μm.

	79.2 mm depth		79.4 mm depth	
	PSL	FWHM	PSL	FWHM
DAS Boxcar	-9.8 dB	529.1 μm (2.84λ)	-12.9 dB	743.1 μm (4λ)
DAS Hanning	-19.9 dB	893.8 μm (4.81λ)	-18.9 dB	844.3 μm (4.54λ)
MV	-18.1 dB	120.9 μm (0.65λ)	-22.5 dB	82.7 μm (0.44λ)

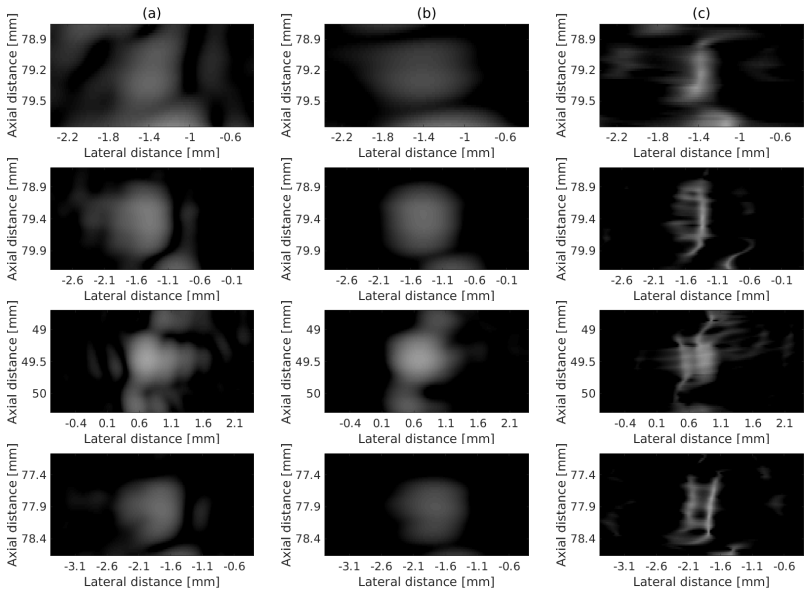

Fig. 10. Beamformed responses of potentially individual MBs (first 2 rows) and double MB scattering events (last 2 rows) at various depths, with (a) DAS Boxcar, (b) DAS Hanning, and (c) MV apodization. The dynamic range of the display was 40 dB.

Similar to the MBs displayed in rows $1-2$ of Fig. 10, a collection of 10 isolated echoes were identified per processed frame, and studied for all beamformers. The FWHM was measured between 70.9 μm (or 0.38λ) and 202.2 μm (or 1.08λ) using the MV beamformer, and between 389.9 μm (or 2.09λ) and 787.7 μm (or 4.24λ) using the best DAS beamformer (Boxcar). Overall, the lateral resolution gains using the adaptive beamformer varied greatly and were calculated between 2-fold and 9-fold. The PSL achieved by the MV beamformer was between -22 dB and -9 dB and on average ≈ 2 dB

This article has been accepted for publication in a future issue of this journal, but has not been fully edited. Content may change prior to final publication. Citation information: DOI 10.1109/TMI.2018.2859262, IEEE Transactions on Medical Imaging

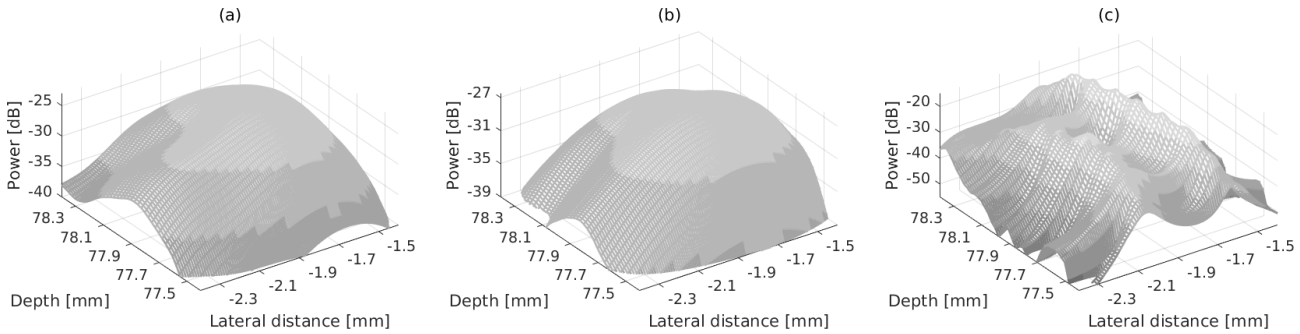

Fig. 11. Lateral variations between 77.4 mm and 78.4 mm depths of the beamformed responses of Fig. 10 (4^{th} row) using (a) DAS Boxcar, (b) DAS Hanning, and (c) MV apodization.

lower compared with the best DAS beamformer (Hanning) that provided values between -20 dB and -7 dB. Given the high MB density, it is highly likely that several scattering events and the increased FWHM variability are due to the presence of more than one scatterers. Thus, a correlation with depth for all beamformers similar to that found in Figs. 6 and 7 was not found here.

In addition, in the MB experimental data there were several cases, where 2 scattering events next to each other, were clearly distinguished in the MV image, while there was only one scattering event displayed in the corresponding DAS images. Such events occured in the depths of 49.5 mm, 51.7 mm, 59.3 mm, 63.2 mm, and 80.1 mm in Fig. 9. Fig. 10 (rows $3-4$) shows two typical examples of possible double MB events identified among the frames. In Fig. 11 the lateral variations for 1 mm depth range are shown for all beamformers for the beamformed responses at the 4^{th} row of Fig. 10. The lateral variations in Fig. 11(a)-(b) suggest that a single scatterer is shown in the 4^{th} row of Fig. 10(a)-(b) while there are at least two visible peaks in Fig. 10(c), using the MV beamformer. Unlike the simulation study of the previous section, the scatterers' positions were not known. The lateral separation may be estimated by the distance between the two distinct peaks, as in Fig. 11(c). This lateral distance was found equal to 225 μm (or 1.21λ) for the scatterer responses positioned at 49.5 mm depth, and to 291 μm (or 1.56λ) for those positioned at 77.9 mm depth. Furthermore, the tilting shown in MB pairs (last two rows of Fig. 10) is in direct comparison with the simulation results where there was a separation in the axial (z) or out-of-plane (y) directions (Fig. 2(d)-(e)). The elongated axial size of the scatterer response shown in Fig. 10 (rows 2, 4) may also be due to the axial distance between merged scatterers as shown in (Fig. 2(d)). The power range is significantly higher in Fig. 11(c) for the MV beamformer (36 dB) compared to the best DAS (Boxcar, 17 dB) in Fig. 11(a). This shows that the scattering events are more clearly defined using the MV beamformer, and also that the MV responses have higher capacity to increase the dynamic range. On average and using the same dynamic range, there were at least 4 clear cases per frame, where 2 closely spaced MB echoes were perceived as individual scatterers using the MV beamformer, while they appeared as a single one using the standard DAS beamformers. The lateral distances between the two echoes varied for the entire dataset between 196.1 μm (or 1.05λ) and 375.2 μm (or 2.02λ). The former value indicates the lateral resolution of the MV beamformer in the current measurement. The experiment was designed, so that there is no scatterer separation using the DAS beamformers. Therefore their separation limit could not be defined experimentally, but was definitely poorer than 400 μm (or 2.15λ) as explained in Subsection II-B3. These results are in quantitative agreement with the simulation results.

IV. Discussion

The MV beamformer was deployed here using simulated point scatterers and flowing MBs, acquired from single emissions and resulted in images of these targets with sub-wavelength lateral FWHM (0.37λ), which is an almost 8-fold improvement compared to conventional beamforming. This is in agreement with previous work on linear scatterers both in simulation and in a wire-target phantom [10]–[12]. However, the experimentally measured FWHM varied amongst the MB echoes, as it is likely that they were due to multiple MBs. Further, the MV implementation employed here included diagonal loading during the adaptive apodization weight calculation (subsection II-A). This reduced visible interference patterns due to the lower scatterer amplitudes. However, by doing so and increasing the robustness of the sample covariance matrix estimate, the lateral resolution is compromised as there is a trade-off between the two [6]. As a consequence the FWHM values obtained were increased compared to those reported in [10]–[12], where values as low as 20 μm were achieved. The rationale for choosing the specific MV beamformer parameters stems from the need to have simulations and measurements that are processed in a similar manner as this enables their comparison. In general, the MV beamformer can provide images of isolated point scatterers at super-resolution. In this work it was also shown that the lateral resolution of the MV beamformer (S_{-3dB}), was found similar to the wavelength (0.91λ), while the S_{-3dB} for the DAS beamformers was more than double (2.08λ). Note that the critical scatterer separation (S_{-3dB}) was adopted as the lateral resolution limit to enable objective comparisons. However, it was shown that detectable separation is possible to a different degree for the different beamformers.

The simulation clarified on how the size or appearance of the scatterer response is affected when two scatterers are placed very closely. Apart from the scatterer distance, the

This article has been accepted for publication in a future issue of this journal, but has not been fully edited. Content may change prior to final publication. Citation information: DOI 10.1109/TMI.2018.2859262, IEEE Transactions on Medical Imaging

depth and number of scatterers are important. These may affect the size and intensity of the main lobe as in the case of Hanning and MV beamformers (Fig. 2(b) and (c)) and may introduce significant side-lobes as for the Boxcar beamformer (Fig. 2(a)). The different sizes and appearances of scattering events shown in simulations justify the large FWHM variability that appeared in the experiments. An additional cause for the FWHM variability was shown in Fig. 5, where the FWHM was found to be dependent on the distance between the two well-separated single scatterers for distances higher than S_{-6dB} ($\approx 2\lambda$). This is not attributed particularly to the MV beamformer, but rather on the interaction of the main lobes between two point scatterers. Fig. 5 shows that while at large lateral distances scatterers provide $\approx \lambda/2$ FWHM values (as in the case of isolated scatterers), their approach increases their FWHM to $\approx 1.3\lambda$ at S_{-6dB}. Thus, a distance of a few wavelengths (Fig. 5 maximum in x-axis is 1 mm $\approx 5\lambda$) between single scatterers significantly affects their size in the image. This effect is also responsible for the eventual "PSF tilting". As one of the two scatterers is slightly closer to the transducer compared to its counterpart, the interaction between the main lobes of the scatterers in the pair will affect (Fig. 2(d)-(e)) the angle of the PSF.

The FWHM is often used in the literature as a proxy for system resolution. Figs. 6 and 8 show that there is a complex relation between FWHM and the resolving capability of each beamformer. While a single isolated scatterer can have a constant FWHM with depth using the MV beamformer (Fig. 6(a)), the system resolution deteriorates with depth (Fig. 8), which is attributed to the divergence of the beam in this case. This is also shown in the FWHM of each scatterer in S_{-6dB} (Fig. 6(c)). On the other hand the DAS beamformers showed that the FWHM of isolated single scatterers increased with depth (Fig. 6(a)), which indicates a more consistent behaviour with beam divergence compared to the MV beamformer. Further, for the DAS beamformers the correlation with depth in Fig. 6(c) is relatively similar to that in Fig. 8(a) (S_{-3dB}). These results also demonstrate that MV beamforming effectively contains a dynamic focusing element and that the FWHM must be used with caution and generally cannot substitute the classical definition of resolution. To examine the relation of S_{-3dB} and FWHM further, the ratio of S_{-3dB} to FWHM at S_{-6dB} was plotted over depth in Fig. 12.

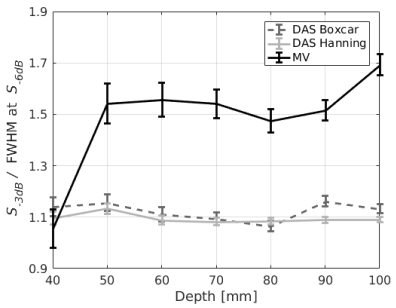

Fig. 12. Critical separation limit (S_{-3dB}) and FWHM at significant separation limit (S_{-6dB}) ratio variation as a function of depth for DAS and MV responses.

The lower S_{-3dB} of the MV beamformer compared to DAS came as a result of the significantly lower FWHM values. This kept the ratio of the above quantities approximately around 1.5 except for the closest to the surface depth (40 mm), where the MV resolving capability is highest. For the DAS beamformers the ratio is slightly above unity (≈ 1.1) and does not depend on depth. In other words, this relative comparison shows that the FWHM at S_{-6dB} may be a good approximation of the lateral resolution using conventional beamformers. However, this did not apply for the MV beamformer. The monotonic increase of the FWHM as scatterers approach in Fig. 5 strongly suggests that further approach towards the S_{-3dB} provides further increase in the FWHM value (if assumed that it is possible to measure) and finally the FWHM converges to the S_{-3dB}. This hypothetical FWHM is equal to the system resolution. Fig. 12 suggests that the FWHM convergence is different for each beamformer, and shows that the MV provided better resolved scatterers compared to the DAS even at short distances (S_{-3dB}) between them. This difference is attributed to the different shape of the main lobe, shown in Fig. 3. By using the MV processing the main lobe widens significantly below -30 dB power and away from its centre (Fig. 3(a)). This appearance is distinctly different to the DAS, where the power drop is steep. Thus, the approach between two scatterers will affect each others FWHM differently for the different beamformers, due to the main lobe overlap effect difference. By definition the FWHM measures the width only at half maximum and thus is not a global measurement for system resolution. Further, comparison between FWHM measurements implies the assumption that the main lobe follows the same function, which is not the case here. The FWHM in conjunction with the system resolution measurement, helps indicate that, compared to the DAS, the MV beamformer may enable a better scatterer detection when in close proximity to others. On the other hand, the experimentally measured PSL did not show agreement with the simulation. While the simulation result showed some contrast benefits that could reach up to -20 dB in non-recurring cases in favour of the MV beamformer compared to the best DAS (Hanning), this result was not reproduced in the experiment. Possible reasons may include the overlap and the vicinity of scatterers as described above. In addition, the PSL was not related to the resolving capability of a beamformer. The DAS boxcar beamformer showed lower FWHM values while the DAS Hanning showed improved PSL. However, Fig. 8 shows that DAS Boxcar outperformed DAS Hanning in the scatterer separation limit, pointing out the significance of low FWHM values.

The simulation results on lateral resolution, compare well with the experimental ones and invite further work with ultrasound contrast MBs. The experiment naturally lacks MB position control. Thus the presence of two or more scatterers separated by small distances ($<<\lambda$) in any of the 3 directions is likely. Simulating all possible shapes and orientations of scatterer appearance is only theoretically possible but not practically achievable. Differences between scatterer amplitudes were not incorporated in the simulation, as equal amplitudes improve clarity and help appreciate the appearance of the experimental scatterers. It is known that the varying MB sizes or physical composition introduce a large variability in their response. Further, their position in relation to the centre of

the beam also affects their response as their scattering cross section is dependent on the acoustic pressure. Thus, the range of detected MB amplitudes in an experiment varies from the noise level to a maximum (e.g. for a resonant bubble at a position of maximum acoustic pressure amplitude). The challenge of introducing this complexity into the simulation setup is not necessary for beamforming design. Note that the lowest FWHM measured was 71.9 μm, which is considerably larger than the actual MB size ($1-10$ μm). For the purposes of this work the adjustment of the brightness in the simulation to that of the experiment was adequate and resulted in similar FWHM and resolution results. In addition, the scatterer centres used in all calculations, were based on estimates drawn by the experimental images.

The MV method may provide a beamforming technique tailored to the detection and tracking of MBs to generate super-resolution ultrasound maps. The work here strongly suggests that a larger number of MBs will be measured per frame, not only due to the lateral resolution improvements but also due to the increased PSF brightness, which may facilitate the use of lower intensity thresholds during the image binarization stage [23]. These are likely to improve the quantification of MB track density and reduce the number of frames required to achieve the desired image reconstruction with super-resolution. Future research on the MV beamformer should focus on optimizing MB localization in *in-vivo* measurements incorporating phase or amplitude modulation transmission schemes, which are employed in SRI. The present findings show that isolated single scatterers provide low FWHM values and very low FWHM variation with depth. Potentially an image with sparse scatterers can confirm the knowledge of the FWHM values across the image. For instance, small FWHM values (here $< \lambda/2$) may be eventually identified as single scatterers and greater FWHM values as two or more scatterers that are within a very close distance to each other. Once the scatterer distance increases their joint FWHM widens (before they appear split). Also, the FWHM of a single scatterer widens if another scatterer is approaching. However, the knowledge of scatterers in vicinity is available in the image, and can potentially be used to tell the difference between the two cases. The improvement of resolution using the MV beamformer appears to come at the expense of loss of shape or symmetry which might require a more sophisticated approach to compensate for it. Here the fundamental cases of scatterers in an SRI imaging scenario have been presented: (1) isolated point scatterers, (2) two closely spaced but merged point scatterers and (3) two closely spaced but separated point scatterers. Any combination of these may occur in a real imaging scenario, but the interactions between these for more than 2 MBs are covered by (2) and (3). Thus, the various shapes and orientations may be predicted by a model. This may lead to recovering the centre of a point scatterer more accurately than the centre of mass that includes a gross assumption on the shape of the particle. Of course, the combinations are many and add to the complexity. Alternatively, the above knowledge may also inform the case that the MB location carries a large uncertainty and may be used to reject such data. The elements that constitute the problem are well-defined here and a model of the 3D shape of a point scatterer may be built on the knowledge achieved in this work.

V. Conclusion

A quantitative study of the lateral resolution limit of the Minimum Variance (MV) beamformer was performed on simulated and real ultrasound data. Using microbubble (MB) data from single emissions, the resulting scattered echoes allowed the visualization of closely spaced MBs, separated by down to $\approx \lambda$ distances, which was not possible using conventional beamforming. The scatterer separation limit was reduced by up to 1.5λ for the MV method compared to that achieved by conventional Delay-and-Sum (DAS) beamformers. Furthermore using the MV beamformer, the FWHM increased as two scatterers approached each other laterally, and slight differences in their axial or out-of-plane position may cause "PSF tilting" for both scatterers. These results explain the variable echo appearance observed in the experimental data and suggest that an increased localization accuracy may be achieved in applications that deploy point scatterers as in MB-based ultrasound super-resolution.

Acknowledgment

The authors would like to thank Prof. Alexander L. Klibanov (University of Virginia, VA, USA) for kindly providing the microbubbles used for the experimental measurements, and Dr. Steve Pye (Medical Physics, NHS Lothian, UK) for valuable discussions.

References

[1] K. E. Thomenius, "Evolution of ultrasound beamformers," in *Proc. IEEE Ultrason. Symp.*, vol. 2, Nov. 1996, pp. 1615–1622.

[2] V. Sboros, C. M. Moran, S. D. Pye, and W. N. McDicken, "The behaviour of individual contrast agent microbubbles," *Ultr. Med. Biol.*, vol. 29, no. 5, pp. 687–694, 2003.

[3] S. Haykin, J. H. Justice, N. L. Owsley, J. L. Yen, and A. C. Kak, *Array signal processing*. Englewood Cliffs, NJ: Prentice Hall, 1985.

[4] J. Capon, "High-resolution frequency-wavenumber spectrum analysis," *Proc. IEEE*, vol. 57, no. 8, pp. 1408–1418, Aug. 1969.

[5] Z. Wang, J. Li, and R. Wu, "Time-delay- and time-reversal-based robust Capon beamformers for ultrasound imaging," *IEEE Trans. Medical Imaging*, vol. 24, no. 10, pp. 1308–1322, 2005.

[6] J. F. Synnevåg, A. Austeng, and S. Holm, "Adaptive beamforming applied to medical ultrasound imaging," *IEEE Trans. Ultrason., Ferroelectr., Freq. Control*, vol. 54, no. 8, pp. 1606–1613, Aug. 2007.

[7] F. Vignon and M. R. Burcher, "Capon beamforming in medical ultrasound imaging with focused beams," *IEEE Trans. Ultrason., Ferroelectr., Freq. Control*, vol. 55, no. 3, pp. 619–628, Mar. 2008.

[8] J. F. Synnevåg, A. Austeng, and S. Holm, "Benefits of minimum variance beamforming in medical ultrasound imaging," *IEEE Trans. Ultrason., Ferroelectr., Freq. Control*, vol. 56, no. 9, pp. 1868–1879, Sep. 2009.

[9] I. K. Holfort, F. Gran, and J. A. Jensen, "Broadband minimum variance beamforming for ultrasound imaging," *IEEE Trans. Ultrason., Ferroelectr., Freq. Control*, vol. 56, no. 2, pp. 314–325, Feb. 2009.

[10] K. Diamantis, I. H. Voxen, A. H. Greenaway, T. Anderson, J. A. Jensen, and V. Sboros, "A comparison between temporal and subband minimum variance adaptive beamforming," in *Proc. SPIE Med. Imag.*, vol. 90400L, Mar. 2014. [Online]. Available: 10.1117/12.2043602.

[11] J. Zhao, Y. Wang, J. Yu, W. Guo, T. Li, and Y.-P. Zheng, "Subarray coherence based postfilter for eigenspace based minimum variance beamformer in ultrasound plane-wave imaging," *Ultrasonics*, vol. 65, pp. 23–33, 2016.

[12] K. Diamantis, A. Greenaway, T. Anderson, J. A. Jensen, and V. Sboros, "Experimental performance assessment of the sub-band minimum variance beamformer for ultrasound imaging," *Ultrasonics*, vol. 79, pp. 87–95, 2017.

[13] A. C. Jensen and A. Austeng, "An approach to multibeam covariance matrices for adaptive beamforming in ultrasonography," *IEEE Trans. Ultrason., Ferroelectr., Freq. Control*, vol. 59, no. 6, pp. 1139–1148, June 2012.

[14] B. M. Asl and A. Mahloojifar, "Contrast enhancement and robustness improvement of adaptive ultrasound imaging using forward-backward minimum variance beamforming," *IEEE Trans. Ultrason., Ferroelectr., Freq. Control*, vol. 58, no. 4, pp. 858–867, 2011.

[15] J. P. Asen, A. Austeng, and S. Holm, "Capon beamforming and moving objects - An analysis of lateral shift-invariance," *IEEE Trans. Ultrason., Ferroelectr., Freq. Control*, vol. 61, no. 7, pp. 1152–1160, July 2014.

[16] N. Q. Nguyen and R. W. Prager, "Minimum variance approaches to ultrasound pixel-based beamforming," *IEEE Trans. Medical Imaging*, vol. 36, no. 2, pp. 374–384, Feb 2017.

[17] H. Taki, K. Taki, T. Sakamoto, M. Yamakawa, T. Shiina, M. Kudo, and T. Sato, "High range resolution ultrasonographic vascular imaging using frequency domain interferometry with the Capon method," *IEEE Trans. Medical Imaging*, vol. 31, no. 2, pp. 417–429, Feb. 2012.

[18] B. Y. Yiu and A. C. Yu, "GPU-based minimum variance beamformer for synthetic aperture imaging of the eye," *Ultr. Med. Biol.*, vol. 41, no. 3, pp. 871–883, 2015.

[19] J. P. Asen, J. I. Buskenes, C. I. C. Nilsen, A. Austeng, and S. Holm, "Implementing Capon beamforming on a GPU for real-time cardiac ultrasound imaging," *IEEE Trans. Ultrason., Ferroelectr., Freq. Control*, vol. 61, no. 1, pp. 76–85, Jan. 2014.

[20] O. M. H. Rindal, S. Aakhus, S. Holm, and A. Austeng, "Hypothesis of improved visualization of microstructures in the interventricular septum with ultrasound and adaptive beamforming," *Ultr. Med. Biol.*, vol. 43, no. 10, pp. 2494–2499, Oct. 2017.

[21] M. Tanter and M. Fink, "Ultrafast imaging in biomedical ultrasound," *IEEE Trans. Ultrason., Ferroelec., Freq. Contr.*, vol. 61, no. 1, pp. 102–119, 2014.

[22] M. A. O'Reilly, R. M. Jones, and K. Hynynen, "Three-dimensional transcranial ultrasound imaging of microbubble clouds using a sparse hemispherical array," *IEEE Trans. Biom. Eng.*, vol. 61, no. 4, pp. 1285–1294, 2014.

[23] K. Christensen-Jeffries, R. J. Browning, M. X. Tang, C. Dunsby, and R. J. Eckersley, "*In vivo* acoustic super-resolution and super-resolved velocity mapping using microbubbles," *IEEE Trans. Medical Imaging*, vol. 34, no. 2, pp. 433–440, Feb. 2015.

[24] C. Errico, B. F. Osmanski, S. Pezet, O. Couture, Z. Lenkei, and M. Tanter, "Transcranial functional ultrasound imaging of the brain using microbubble-enhanced ultrasensitive doppler," *NeuroImage*, vol. 124, no. Pt A, pp. 752–761, 2015.

[25] D. Ackermann and G. Schmitz, "Detection and tracking of multiple microbubbles in ultrasound b-mode images," *IEEE Trans. Ultrason., Ferroelec., Freq. Contr.*, vol. 63, no. 1, pp. 72–82, Jan. 2016.

[26] P. Hoskins, K. Martin, and A. Thrush, *Diagnostic ultrasound: Physics and equipment*, 2nd ed. Cambridge University Press, 2010.

[27] S. Mehdizadeh, A. Austeng, T. F. Johansen, and S. Holm, "Eigenspace based minimum variance beamforming applied to ultrasound imaging of acoustically hard tissues," *IEEE Trans. Medical Imaging*, vol. 31, no. 10, pp. 1912–1921, Oct 2012.

[28] F. J. Harris, "On the use of windows for harmonic analysis with the discrete fourier transform," *Proc. IEEE*, vol. 66, no. 1, pp. 51–83, 1978.

[29] S. I. Nikolov, J. A. Jensen, and B. G. Tomov, "Fast parametric beamformer for synthetic aperture imaging," *IEEE Trans. Ultrason., Ferroelectr., Freq. Control*, vol. 55, no. 8, pp. 1755–1767, Aug. 2008.

[30] C. H. Frazier and W. D. O'Brien, "Synthetic aperture techniques with a virtual source element," *IEEE Trans. Ultrason., Ferroelectr., Freq. Control*, vol. 45, no. 1, pp. 196–207, Jan 1998.

[31] N. Oddershede and J. A. Jensen, "Effects influencing focusing in synthetic aperture vector flow imaging," *IEEE Trans. Ultrason., Ferroelectr., Freq. Control*, vol. 54, no. 9, pp. 1811–1825, Sept. 2007.

[32] J. A. Jensen and N. B. Svendsen, "Calculation of pressure fields from arbitrarily shaped, apodized, and excited ultrasound transducers," *IEEE Trans. Ultrason., Ferroelectr., Freq. Control*, vol. 39, pp. 262–267, 1992.

[33] J. A. Jensen, "Field: A program for simulating ultrasound systems," *Med. Biol. Eng. Comp., vol. 10th Nordic-Baltic Conference on Biomedical Imaging, Supplement 1, Part 1*, vol. 4, pp. 351–353, 1996.

[34] V. Sboros, C. M. Moran, S. D. Pye, and W. N. McDicken, "An in vitro study of a microbubble contrast agent using a clinical ultrasound imaging system," *Phys. Med. Biol.*, vol. 49, no. 1, pp. 159–173, 2004.

[35] J. A. Jensen, H. Holten-Lund, R. T. Nilsson, M. Hansen, U. D. Larsen, R. P. Domsten, B. G. Tomov, M. B. Stuart, S. I. Nikolov, M. J. Pihl, Y. Du, J. H. Rasmussen, and M. F. Rasmussen, "SARUS: A synthetic aperture real-time ultrasound system," *IEEE Trans. Ultrason., Ferroelectr., Freq. Control*, vol. 60, no. 9, pp. 1838–1852, 2013.

[36] W. Marczak, "Water as a standard in the measurements of speed of sound in liquids," *J. Acoust. Soc. Am.*, vol. 102, no. 5, pp. 2776–2779, 1997.

[37] A. L. Klibanov, P. T. Rasche, M. S. Hughes, J. K. Wojdyla, K. P. Galen, J. H. J. Wible, and G. H. Brandenburger, "Detection of individual microbubbles of ultrasound contrast agents: imaging of free-floating and targeted bubbles." *Invest. Radiol.*, vol. 39, no. 3, pp. 187–195, 2004.

[38] V. Sboros, C. M. Moran, T. Anderson, and W. N. McDicken, "An in vitro comparison of ultrasonic contrast agents in solutions with varying air levels," *Ultr. Med. Biol.*, vol. 26, no. 5, pp. 807 – 818, 2000.

[39] J. A. Jensen, M. F. Rasmussen, M. J. Pihl, S. Holbek, C. A. V. Hoyos, D. P. Bradway, M. B. Stuart, and B. G. Tomov, "Safety assessment of advanced imaging sequences I: measurements," *IEEE Trans. Ultrason., Ferroelec., Freq. Contr.*, vol. 63, no. 1, pp. 110–119, 2016.